



An X-Ray Burst Associated with FRB 200428 from a Magnetar-asteroid Impact

Ze-Nan Liu^{1,2}, Yuan-Pei Yang³, Wei-Yang Wang^{4,5}, Zhao Joseph Zhang^{1,2}, Qiao-Chu Li^{1,2}, Ken Chen^{1,2}, Jia Ren^{1,2}, Bin-Bin Zhang^{1,2}, Cheng-Kui Li⁶, Shuang-Nan Zhang^{4,6}, and Zi-Gao Dai^{1,7}

¹School of Astronomy and Space Science, Nanjing University, Nanjing 210023, China

²Key Laboratory of Modern Astronomy and Astrophysics (Nanjing University), Ministry of Education, Nanjing 210023, China

³South-Western Institute for Astronomy Research, Yunnan University, Kunming 650500, China

⁴National Astronomical Observatories, Chinese Academy of Sciences, Beijing 100101, China

⁵University of Chinese Academy of Sciences, Chinese Academy of Sciences, Beijing 100049, China

⁶Key Laboratory of Particle Astrophysics, Institute of High Energy Physics, Chinese Academy of Sciences, Beijing 100049, China

⁷Department of Astronomy, School of Physical Sciences, University of Science and Technology of China, Hefei 230026, China; daizg@ustc.edu.cn

Received 2023 January 21; revised 2023 May 17; accepted 2023 May 19; published 2023 July 5

Abstract

Fast radio bursts (FRBs) are extragalactic radio transients with millisecond duration and brightness temperature. An FRB-associated X-ray burst (XRB) was recently found to arise from the Galactic magnetar SGR J1935+2154. Following the model of Dai, in which an FRB may originate from a magnetar encountering an asteroid, we focus on explaining the spectrum of the XRB associated with FRB 200428 from SGR J1935+2154. Collisions between asteroidal fragments and the magnetar surface produce a fireball, which further expands relativistically. Due to the velocity difference among some shells in the fireball, internal shocks would form far away from the magnetar, and further emit X-ray emission. We propose that the FRB-associated XRB can be produced by synchrotron emission from the internal shocks, and then constrain the physical parameters by the observed XRB spectrum.

Key words: stars: magnetars – minor planets – asteroids: general – radiation mechanisms: general

1. Introduction

Fast radio bursts (FRBs) are a kind of extragalactic radio transient with millisecond duration (Lorimer et al. 2007; Keane et al. 2012; Thornton et al. 2013). So far, many physical models have been proposed to explain FRBs (see details Platts et al. 2019; Xiao et al. 2020; Zhang 2020; Lyubarsky 2021), including close-in models and far-away models based on the distance of the radiation region from the neutron star. For example, the close-in models show that the radio emission comes from the magnetosphere of a neutron star (Cordes & Wasserman 2016; Kumar et al. 2017; Zhang 2017; Ghisellini & Locatelli 2018; Katz 2018; Yang & Zhang 2018; Lu & Kumar 2019; Wang et al. 2019; Wadiasingh & Timokhin 2019; Dai 2020; Geng et al. 2020; Lu et al. 2020; Wadiasingh et al. 2020; Wang et al. 2020; Yang et al. 2020; Zhang 2020; Yang & Zhang 2021), which is supported by the observed light curve variability timescales and the spectro-temporal correlations (Beniamini & Kumar 2020). The far-away models suggest that an outflow interacts with the ambient medium to release energy, and radio emission is generated by synchrotron maser emission (Lyubarsky 2014; Beloborodov 2017; Ghisellini 2017; Waxman 2017; Gruzinov & Waxman 2019; Metzger et al. 2019; Beloborodov 2020; Margalit et al. 2020; Wu et al. 2020; Xiao & Dai 2020).

Very recently, Bochenek et al. (2020) and CHIME/FRB Collaboration et al. (2020b) reported a short radio burst, FRB 200428, with two pulses from the general direction of the Galactic magnetar SGR J1935+2154. The reported FRB 200428 has two pulses with intrinsic durations of 0.60 ms and 0.34 ms, respectively (CHIME/FRB Collaboration et al. 2020b; Bochenek et al. 2020), and the two pulses are separated by ~ 29 ms. Moreover, the intriguing X-ray burst (XRB) associated with FRB 200428, which has two corresponding pulses, was coincidentally observed by high-energy satellites such as Insight-HXMT (Li et al. 2021), INTEGRAL (Mereghetti et al. 2020), Konus-Wind (Ridnaia et al. 2021) and AGILE (Tavani et al. 2021). Remarkably, since Insight-HXMT has the wider energy band observation, the extended low energy emission was observed with Insight-HXMT in the 1–250 keV energy band, and the XRB spectrum is dominated by the non-thermal component (Li et al. 2021). Therefore, in the following discussion, we constrain the model parameters using Insight-HXMT data (see Section 3). Noticeably, the spectrum of the XRB is consistent with other magnetar bursts, but the cutoff energy in this event is significantly higher than the typical burst energy (Ridnaia et al. 2021; Younes et al. 2021). It is suggested that the associated event might be special compared with normal XRBs. Some works considered a trapped fireball and a relativistic outflow to explain the hard XRB (Ioka 2020;

Yamasaki et al. 2022). Subsequently, there were over 217 bursts observed during the first 1120 s from SGR J1935+2154 (Younes et al. 2020), but their characteristics were different from those of the XRB associated with FRB 200428, which exhibited a higher peak energy and a lower flux density at peak energy (Ridnaia et al. 2021; Younes et al. 2021).

Remarkably, some recent works involved the interaction between neutron stars and asteroids in explaining FRBs (Dai 2020; Geng et al. 2020; Decoene et al. 2021). Following Dai (2020), in this work, we propose that the XRB associated with FRB 200428 is produced by synchrotron emission from internal shocks formed by collisions between fast and slow shells produced by a relativistically expanding fireball, which can constrain the model parameters using the observed XRB spectrum. The magnetar-asteroid impact satisfies conservation of energy. The gravitational energy of the asteroid and the magnetic energy of the magnetar's magnetosphere are converted into the kinetic energy of ejected shells. The ejected shell velocity would have some differences after impacting the magnetar's surface due to the components of multipolar fields at the magnetar's surface. In our model, a freely-falling asteroid with a mass of $m_a \sim 10^{20}$ g is impeded by an ultra-strong magnetic field at Alfvén radius R_A , and then some major fragments with a mass of $m \sim 10^{19}$ g move along the magnetic field lines and generate pulses from FRB 200428 and its associated XRB (Dai 2020). This work is organized as follows. We describe the physical process of an expanding fireball generated by the magnetar-asteroid impact in Section 2.1. We analyze the internal shock model to account for the synchrotron emission spectrum in Section 2.2. The best fitting results are shown in Section 3. The results are discussed and summarized in Section 4. The convention $Q_x = Q/10^x$ in cgs units is used throughout this paper.

2. An Expanding Fireball and X-Ray Emission from Internal Shocks

The impact of an asteroid/comet with a neutron star was proposed early as an origin of gamma-ray bursts (GRBs, Colgate & Petschek 1981; Howard et al. 1981; van Buren 1981; Mitrofanov & Sagdeev 1990; Shull & Stern 1995) and soft gamma repeaters (SGRs, Livio & Taam 1987; Boer et al. 1989; Katz et al. 1994). In our model, when an asteroid collides with the polar surface of a magnetar, a conical hot plasma (fireball) is ejected, which is different from the fan-shaped outflow discussed by Colgate & Petschek (1981).

2.1. An Expanding Fireball

We consider an asteroid with a mass of $m_a \sim 10^{20}$ g to freely fall in the gravitational field of a magnetar, which is disrupted tidally into some fragments at $\sim 10^{10}$ cm from the magnetar's center. Some major fragments are distorted tidally at breakup

radius (Colgate & Petschek 1981)

$$R_b = (\rho_0 r_0^2 GM/s)^{1/3} \simeq 3.3 \times 10^8 \text{ cm } m_{19}^{2/9} \rho_{0,0.5}^{1/9} s_{13}^{-1/3} (M/1.4 M_\odot)^{1/3}, \quad (1)$$

where ρ_0 , r_0 , s and M are the iron-nickel asteroid's original mass density, radius, tensile strength and stellar mass, respectively. When an asteroid falls toward the magnetar's surface, electrons are torn off the asteroidal surface by an induced parallel electric field. These accelerated electrons move along magnetic field lines, and emit an FRB by coherent curvature radiation (Dai et al. 2016). Subsequently, some fragments are accreted onto the footpoints of closed magnetic field lines (see Figure 1(a)). A fireball with electrons and baryons is generated during the collision. The fireball expands relativistically due to an extremely high initial temperature, and blackbody emission is generated from the expanding fireball at the photosphere radius (see Figure 1(b)). Synchrotron emission from collisions between different shells in the relativistic fireball produces an XRB (see Figure 1(c)).

When an asteroid is slowed down around the Alfvén radius R_A by an ultra-strong magnetic field of the magnetar, some major fragments with mass $\sim 10^{19}$ g move along magnetic field lines from R_A onto the footpoints of closed magnetic field lines (Dai 2020). For a dipole magnetic field configuration, the radial direction positions (R_*, θ_1) and (R_*, θ_2) signify that the boundary of a fragment corresponds to the surface of the magnetar, where R_* is the surface radius of the magnetar. We have

$$R_{\max} \sin^2 \theta_1 = (R_{\max} + l_a) \sin^2 \theta_2, \quad (2)$$

where $R_{\max} \simeq R_A$, R_{\max} is the maximum distance of magnetic field lines across the equator and l_a is the length of the compressed asteroid. At the Alfvén radius, the kinetic energy density of the fragment is equal to the magnetic energy density, and one has (Dai 2020)

$$R_A = 3.0 \times 10^7 \text{ cm } (\kappa/0.13)^{-1/9} s_{13}^{1/27} \rho_{0,0.5}^{-19/81} \mu_{32}^{4/9} \times m_{19}^{-2/81} (M/1.4 M_\odot)^{-7/27}, \quad (3)$$

where κ is the solid body compressive strength ratio, and the magnetic dipole moment $\mu = B_s R_*^3$ ($B_s \simeq 2.2 \times 10^{14}$ G (Israel et al. 2016)). The asteroidal length can be written as $l_a = l_0 (R/R_b)^{-1/2}$ for $R \leq R_i$ (Colgate & Petschek 1981), where l_0 is the asteroid's original radius and R_i denotes the radius at which compression begins. The length of the asteroid l_a at the Alfvén radius can be estimated by

$$l_a \simeq 5.4 \times 10^6 \text{ cm } m_{19}^{37/81} \rho_{0,0.5}^{-13/81} s_{13}^{-5/27} (\kappa/0.13)^{1/18} \times (M/1.4 M_\odot)^{8/27} \mu_{32}^{-2/9}. \quad (4)$$

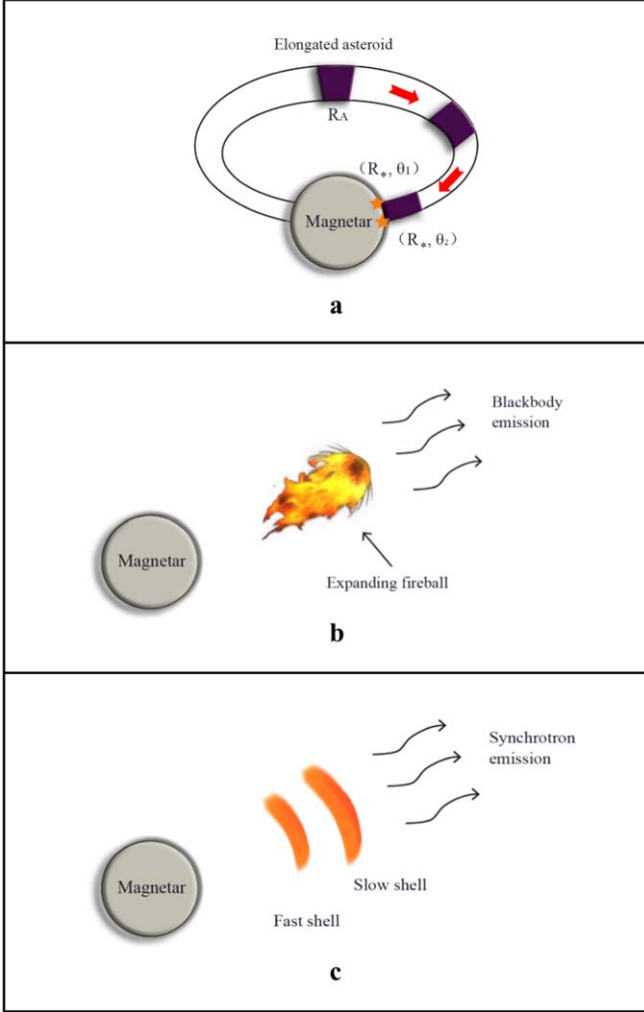


Figure 1. Schematic collision geometry between an elongated, compressed asteroid and a magnetar. (a) Some fragments (we just show one fragment in our picture) freely fall in the gravitational field of the magnetar until the Alfvén radius R_A , and then are accreted onto the footpoints (orange stars) of closed magnetic field lines. The three purple parts illustrate the falling process of a fragment. (b) A fireball is generated by the collision, which then expands relativistically. Blackbody emission is generated from a photosphere. (c) Synchrotron emission from the collisions between different shells produces an XRB. The different fragments would contribute to the different shells.

Combining Equations (2), (3) and (4), the initial size of the trapped fireball $\ell_{0,X}$ can be expressed as

$$\begin{aligned} \ell_{0,X} &= R_*(\theta_1 - \theta_2) \simeq \frac{1}{2} R_*^{3/2} R_A^{-3/2} l_a \\ &\simeq 1.6 \times 10^4 \text{ cm } R_{*,6}^{3/2} m_{19}^{40/81} \rho_{0,0.5}^{31/162} s_{13}^{-13/54} (\kappa/0.13)^{2/9} \\ &\quad \times (M/1.4 M_\odot)^{37/54} \mu_{32}^{-8/9}. \end{aligned} \quad (5)$$

Under the assumption of thermal equilibrium, the temperature of the fireball T_0 can be estimated by

Thompson & Duncan (1995)

$$T_0 \sim \left(\frac{B_s^2}{8\pi a} \right)^{1/4} \simeq 6.1 \times 10^{10} \text{ K} \left(\frac{B_s}{10^{15} \text{ G}} \right)^{1/2}, \quad (6)$$

where $a = 7.56 \times 10^{-15} \text{ erg cm}^{-3} \text{ K}^{-4}$ corresponds to the radiation energy density constant. Since kT_0 is greater than the electron rest energy, the huge optical depth due to photon-photon annihilation reactions in the fireball (see Dai 2020) inevitably generates a dense population of electron and positron pairs and further makes the fireball highly collisional and opaque. The magnetic field on the surface of a magnetar will be higher due to the components of multipolar fields. The higher magnetic field will increase the initial temperature to contribute to blackbody emission from the hot spot that will produce a fireball. Meanwhile, the collisions between different relativistic shells in the fireball can produce non-thermal emission components, which will be discussed in Section 2.2.

After generating a fireball by the collisions, some baryons might be contaminated, similar to the SGR 1806-20 giant flare in 2004 (Granot et al. 2006). According to the conservation of baryon number and energy, we can get the magnitude of bulk Lorentz factor (i.e., the fireball can be accelerated to the maximum Lorentz factor), which is limited by the total entropy per baryon in the fireball as (Yamasaki et al. 2022) $\Gamma_i = 1 + (kT_0/m_e c^2) \simeq 10$, where k is the Boltzmann constant.

Because the fireball pressure is comparable to the magnetic field pressure, the fireball can expand outside along the magnetic field lines. If $R > R_*$, the expanding fireball size ℓ_X evolves as $\ell_X = \ell_{0,X} (R/R_*)^{3/2}$ in the magnetosphere of a magnetar (Thompson & Duncan 1995). The Lorentz factor evolves as $\Gamma \propto \ell_X$, and the temperature of the fireball evolves as $T \propto \ell_X^{-1}$ during adiabatic expansion (Thompson & Duncan 2001). The bulk Lorentz factor and comoving temperature of the expanding fireball evolve as

$$\Gamma = \begin{cases} \Gamma_0 (R/R_*)^{3/2}, & R \leq R_c, \\ \Gamma_i, & R > R_c. \end{cases} \quad (7)$$

$$T = \begin{cases} T_0 (R/R_*)^{-3/2}, & R \leq R_c, \\ T_0 (R_*/R_c)^{1/2} (R/R_*)^{-1}, & R > R_c. \end{cases} \quad (8)$$

Here Γ_0 denotes the initial Lorentz factor of the fireball. We define the maximum acceleration radius $R_c \simeq 5 \times 10^6 \text{ cm}$ for $\Gamma \simeq \Gamma_i$. The fireball keeps moving at a constant Lorentz factor with Γ_i for $R > R_c$. When the fireball moves to $R > R_c$, in the matter-dominated phase, the temperature of the expanding fireball evolves as $T \propto \ell_X^{-2/3}$, thus, we can get $T = T_0 (R_*/R_c)^{1/2} (R/R_*)^{-1}$ ($R > R_c$). The fireball can be accelerated to the maximum Lorentz factor (Γ_i), which would decide the maximum acceleration radius, and further affects the evolution of the Lorentz factor and temperature of the expanding fireball. From another point of view, we obtain the maximum Lorentz factor of the fireball as follows. The collision

process satisfies conservation of energy. The gravitational energy of the asteroid and the magnetic energy of the magnetar's magnetosphere are converted into the kinetic energy of ejected shells. If we consider the energy conversion efficiency η , one has $\eta(E_B + E_G) = E_K$. Assuming that the volume of magnetosphere energy dissipation is comparable to the asteroidal volume near the surface of a magnetar, the magnetic energy of the magnetar's magnetosphere $E_B = VB_s^2/8\pi \simeq 8 \times 10^{41} B_{s,14}^2 r_{a,4}^2 l_{a,7} \text{ erg}$, where $V = \pi r_a^2 l_a$, and r_a and l_a denote the radius and length of the asteroid, respectively (Colgate & Petschek 1981). The gravitational energy of the asteroid $E_G = GMm_a/R_* \simeq 1.9 \times 10^{40} m_{a,20} (M/1.4 M_\odot) R_{*,6}^{-1} \text{ erg}$, where m_a is the total asteroidal mass. The kinetic energy of an ejected shell is given by $E_K = \gamma_{\text{shell}} M_{\text{shell}} c^2$, where M_{shell} is the ejected shell mass. Consequently, the Lorentz factor of the ejected shell can be estimated by

$$\gamma_{\text{shell}} \simeq 8.3 \eta_{-1} B_{s,14}^2 r_{a,4}^2 l_{a,7} m_{a,20} (M/1.4 M_\odot) R_{*,6}^{-1} M_{\text{shell},19}^{-1}. \quad (9)$$

We find γ_{shell} is comparable to Γ_i , indicating that our derivation is self-consistent. As shown in Equation (9), the mass range of each shell will be affected by the Lorentz factor of the ejected shell. If the shell mass is too large, it is hardly accelerated to relativistic velocity. If the shell mass is too small, the Lorentz factor of the ejected shell will be larger than the maximum Lorentz factor. It is not consistent with Equation (6). Thus, the shell mass should be limited by the maximum Lorentz factor. Asteroids would fall randomly into different positions on the magnetar surface. Even though the relative collision location of different fragments is random, the fireball will expand along the open magnetic field lines, resulting in a consistent velocity direction for different fireballs. However, some differences in the magnetic field would exist due to the components of multipolar fields from the magnetar surface. The ejected shell velocity would have some differences. Therefore, internal shocks can be generated by the collisions between fireballs.

When the fireball moves to the photosphere radius, the Thomson optical depth can be given by $\tau_T \approx Zn'_e \sigma_T R / \Gamma$, where Z is the atomic number, σ_T is the Thomson cross-section and n'_e denotes the comoving baryon number density. For a high-load fireball, electrons and baryons dominate the number density. According to conservation of the electron number density, the radial evolution of the electron number density when $R > R_c$ can be given by Yamasaki et al. (2022)

$$n'_e(R) \approx \frac{aT_0^4 \Gamma_0}{m_p c^2} \left(\frac{Z}{A} \right) \Gamma_i^{-2} (R/R_*)^{-3}, \quad (10)$$

where A is the mass number. The Thomson optical depth becomes thin where the fireball expands to the size of $\ell_x \simeq 3.5 \times 10^5 \text{ cm}$, and we also obtain the temperature at the radius of the photosphere $kT \simeq 7 \text{ keV}$ at $5 \times 10^7 \text{ cm}$. These results are consistent with the fitting parameters (see Section 3).

2.2. X-Ray Emission from Internal Shocks

When a fast shell catches up with a slow shell in front of it, the electrons in the shells are accelerated and produce synchrotron radiation. In general, fast and slow shells would be combined after the collision ends, and the whole process satisfies the conservation of energy and momentum. We assume that the mass, velocity, and Lorentz factor of the fast and slow shell can be expressed as M_2, β_2, γ_2 and M_1, β_1, γ_1 , respectively. The separation distance between the fast and the slow shell can be expressed by $c\delta t$, where $\delta t \sim 0.3 \text{ s}$ corresponds to the time of light variable structure (Mereghetti et al. 2020; Li et al. 2021; Ridnaia et al. 2021; Tavani et al. 2021). The shell collision radius is (Paczynski & Xu 1994; Rees & Meszaros 1994)

$$R_{\text{int}} = \frac{c\delta t}{\beta_2 - \beta_1} = \frac{2\gamma_1^2 \gamma_2^2}{\gamma_2^2 - \gamma_1^2} c\delta t. \quad (11)$$

From the time of light variables, we can get the collision radius: $R_{\text{int}} \simeq 5 \times 10^{10} \text{ cm}$. Below, we adopt physical parameters: $\gamma_1 = 2, \gamma_2 = 10$ and $\delta t \simeq 0.3 \text{ s}$. According to the conservation of energy and momentum (Paczynski & Xu 1994), the velocity, Lorentz factor and the internal random motion Lorentz factor can be given by

$$\begin{aligned} M_1 \gamma_1 + M_2 \gamma_2 &= (M_1 + M_2) \gamma_{\text{int}} \gamma, \\ M_1 \gamma_1 \beta_1 + M_2 \gamma_2 \beta_2 &= (M_1 + M_2) \gamma_{\text{int}} \gamma \beta, \end{aligned} \quad (12)$$

and then we can get the β, γ and γ_{int}

$$\begin{aligned} \beta &= \frac{M_1 \gamma_1 \beta_1 + M_2 \gamma_2 \beta_2}{M_1 \gamma_1 + M_2 \gamma_2}, \\ \gamma &= \sqrt{\frac{M_1 \gamma_1 + M_2 \gamma_2}{M_1 / \gamma_1 + M_2 / \gamma_2}}, \\ \gamma_{\text{int}} &= \frac{\sqrt{(M_1 + M_2)^2 + M_1 M_2 (\gamma_1 / \gamma_2 + \gamma_2 / \gamma_1 - 2)}}{M_1 + M_2}. \end{aligned} \quad (13)$$

If we assume the shell that is released has the same mass each time ($M_{\text{shell}} \simeq M_1 \simeq M_2$), γ_{int} can be written as $\gamma_{\text{int}} \simeq (\gamma_1 + \gamma_2) / (2\sqrt{\gamma_1 \gamma_2})$. The stronger the internal shock (i.e., the larger γ_{int}) is, the more internal energy will be generated. The electron energy distribution is assumed to have a power law form: $dn_e/d\gamma_e \propto \gamma_e^{-p}$ for $\gamma_e > \gamma_m$. We assume that ϵ_e is the fraction of the dissipated energy that is carried by leptons in the internal shock and a fraction ϵ_B of the dissipated energy is carried in the form of magnetic fields (Paczynski & Xu 1994). The electron number density and energy density can be expressed as $n_e = n_p = \int_{\gamma_m}^{\gamma_{\text{max}}} n(\gamma_e) d\gamma_e \approx \frac{C}{p-1} \gamma_m^{1-p}$ and $e_e = \epsilon_e e_{\text{int}} = \int_{\gamma_m}^{\gamma_{\text{max}}} \gamma_e m_e c^2 n(\gamma_e) d\gamma_e \approx \frac{C}{p-2} \gamma_m^{2-p} m_e c^2$ respectively, where the internal energy density $e_{\text{int}} = (\gamma_{\text{int}} - 1) n_p m_p c^2$, γ_{max} is the maximum Lorentz factor and C is the constant. We assume $\gamma_{\text{max}} \gg \gamma_m$ and $p > 2$. Then, we can get the minimum electron Lorentz factor (Sari et al. 1998;

Dai & Lu 2002)

$$\gamma_m = \bar{\epsilon}_e(\gamma_{\text{int}} - 1)m_p/m_e, \quad \bar{\epsilon}_e \equiv \epsilon_e(p - 2)/(p - 1), \quad (14)$$

where m_p is the proton mass. The kinetic energy of the shell will be converted into internal energy, which can be written as $E_{\text{shell}}(\gamma_{\text{int}} - 1)/\gamma_{\text{int}}$, where $(\gamma_{\text{int}} - 1)/\gamma_{\text{int}}$ is the conversion efficiency. One can obtain the magnetic energy $\epsilon_B E_{\text{shell}}(\gamma_{\text{int}} - 1)/\gamma_{\text{int}}$, and the magnetic energy density $B^2/8\pi$. Thus, the comoving magnetic field can be given by Zhang & Mészáros (2002)

$$B = \left[\frac{2\epsilon_B E_{\text{shell}}(\gamma_{\text{int}} - 1)}{\gamma_{\text{int}} c \delta t} \right]^{1/2} \frac{1}{\gamma R_{\text{int}}}, \quad (15)$$

where E_{shell} is the shell energy. The characteristic frequency of synchrotron radiation at an electron Lorentz factor γ_e corresponds to photon energy

$$\nu(\gamma_e) = \frac{3x_p}{4\pi} \frac{eB}{m_e c} \gamma_e^2 \gamma_{\text{int}}, \quad (16)$$

where $x_p \approx 0.3$. The characteristic frequency of synchrotron radiation at γ_m and γ_c can be expressed as $\nu(\gamma_m) = 3x_p eB \gamma_m^2 \gamma_{\text{int}}/4\pi m_e c$, and $\nu(\gamma_c) = 3x_p eB \gamma_c^2 \gamma_{\text{int}}/4\pi m_e c$, respectively. The cooling Lorentz factor can be written as $\gamma_c = 6\pi m_e c / \sigma_T B^2 \delta t \gamma_{\text{int}}$. Then, the peak spectral power can be given by Sari et al. (1998)

$$P_{\nu, \text{max}} = \frac{m_e c^2 \sigma_T}{3e} \gamma_{\text{int}} B. \quad (17)$$

The observed peak flux at distance D from the source $F_{\nu, \text{max}} \equiv N_e P_{\nu, \text{max}}/4\pi D^2$, and the total electron numbers can be written as $N_e = M_{\text{shell}}/m_p$. SGR J1935+2154 is associated with the supernova remnant (SNR) G57.2 + 0.8 (Gaensler 2014). The distance D of the SNR G57.2 + 0.8 was estimated to be in a range of ~ 6.6 to ~ 12.5 kpc (Pavlović et al. 2013; Surnis et al. 2016; Kothes et al. 2018; Zhong et al. 2020; Zhou et al. 2020). Electrons can cool down to γ_c for $\gamma_m > \gamma_c$ (fast cooling case) and $\gamma_c > \gamma_m$ (slow cooling case) (Sari et al. 1998). We compare γ_m and γ_c to decide the fast or slow cooling case. $\gamma_m = \bar{\epsilon}_e(\gamma_{\text{int}} - 1)m_p/m_e \simeq 3.9$ and $\gamma_c = 6\pi m_e c / \sigma_T B^2 \delta t \gamma_{\text{int}} \simeq 10.3$. Below, we adopt typical physical parameters: $\gamma_1 = 2$, $\gamma_2 = 10$, $\epsilon_e = 0.1$, $\epsilon_B = 0.1$, $E_{\text{shell}} = 10^{39}$ erg, $m_{\text{shell}} = 10^{19}$ g and $p = 2.5$. The slow cooling case is suitable for our model due to $\gamma_c > \gamma_m$. Thus, we consider the slow cooling case to fit the spectrum of XRB. We also find the fast cooling case corresponds to the condition of higher shell energy and $\gamma_1 < \gamma_2$. The total energy of the observed XRB from SGR J1935+2154 $\sim 10^{40}$ erg is far less than the energy released by the GRB. Thus, the GRB is always in a fast cooling regime. Moreover, if the shell in front is in a state of non-relativistic motion, it will also cause a fast cooling case. The flux at the observer in the slow cooling case can be given by Gao et al.

(2013),

$$F_\nu = \begin{cases} (\nu_a/\nu_m)^{-(p-1)/2} (\nu/\nu_a)^{5/2} F_{\nu, \text{max}}, & \nu_m < \nu \leq \nu_a, \\ (\nu/\nu_m)^{-(p-1)/2} F_{\nu, \text{max}}, & \nu_a < \nu \leq \nu_c, \\ (\nu_c/\nu_m)^{-(p-1)/2} (\nu/\nu_c)^{-p/2} F_{\nu, \text{max}}, & \nu > \nu_c, \end{cases} \quad (18)$$

where ν_a is the synchrotron self-absorption frequency. A convenient method is to define ν_a by equating the synchrotron and blackbody flux (Sari & Piran 1999; Kobayashi & Zhang 2003; Gao et al. 2013). Thus, we can get the expression $\nu_a = (\gamma_{\text{int}} eB/8\pi m_e^3 c)^{1/4} + p F_{\nu, \text{max}}^{2/4} + p \nu_m^{p-1/4} + p$. In addition, the equivalent hydrogen column n_H in the interstellar absorption model is a free parameter.

3. The Fitting Results

We first describe the data on FRB 200428 and the associated XRB. The isotropic-equivalent emission energy release of the XRB in the soft X-ray to soft gamma-ray energy band is $E_X \sim (0.8-1.2) \times 10^{40} (D/10 \text{ kpc})^2$ erg (Mereghetti et al. 2020; Li et al. 2021; Ridnaia et al. 2021; Tavani et al. 2021). Li et al. (2021) reported the two-temperature blackbody model can be easily rejected, but the blackbody plus power law model can fit the FRB 200428-associated burst spectrum well. In the blackbody plus power law model, the blackbody component has a temperature of $11.32_{-0.56}^{+0.55}$ keV. A non-thermal component and a part of the contribution from the blackbody dominate the XRB spectrum. Li et al. (2021) also found the non-thermal X-ray spectrum of the fits to the cutoff power law, where the cutoff energy $E_{\text{cut}} = 83.89_{-7.55}^{+9.08}$ keV. The spectrum of the XRB is consistent with other magnetar bursts, but the cutoff energy in this event is significantly higher than the typical burst energy (Ridnaia et al. 2021; Younes et al. 2021). In addition, the spectrum becomes hard at the two peaks observed by Insight-HXMT (Li et al. 2021). Interestingly, the onset of the XRB is tens of milliseconds ahead of that of the FRBs (Mereghetti et al. 2020; Li et al. 2021; Ridnaia et al. 2021; Tavani et al. 2021). We compare our fitting results with the observations in this section and discussion.

We restrict our model parameters by the Markov Chain Monte Carlo (MCMC) method with the code PyMultiNest (Buchner et al. 2014). The log-likelihood of these parameters can be given by a fitting statistic of Poisson data with Gaussian background, i.e.,

$$PG(\epsilon_e, \epsilon_B, \gamma_1, \gamma_2, p, N_e, kT, \ell_X, E_{\text{shell}}, n_H) = 2 \sum_i t_s(m_i + f_i) - S_i \ln(t_s m_i + t_s f_i) + \frac{1}{2\sigma_i^2} (B_i - t_b f_i)^2 - S_i (1 - \ln S_i) \chi^2, \quad (19)$$

where

$$f_i = \frac{-(t_s \sigma_i^2 - t_b B_i + t_b^2 m_i)^2 \pm d_i}{2t_b^2}, \quad (20)$$

and

$$d_i = [(t_s \sigma_i^2 - t_b B_i + t_b^2 m_i)^2 - 4 t_b^2 \times (t_s \sigma_i^2 m_i - S_i \sigma_i^2 - t_b B_i m_i)]^{1/2}. \quad (21)$$

Here i represents different data from different channels, S_i the observed counts, B_i the background data and m_i the predicted counts based on our model with current parameters, which has been convolved with the instrumental response matrix. t_s and t_b are the exposure times for the source and background spectra, respectively. By minimizing the PG for a wide range of the parameters, we obtain the distribution of the best-fitting parameters, the central values of which maximize the log-likelihood function.

The spectrum of the XRB is displayed in Figure 2. The slow-cooling synchrotron radiation model and blackbody radiation can fit the spectrum well. The spectrum is mainly dominated by synchrotron emission, and the blackbody emission contribution is less significant. The upper limit of the optical flux during the prompt phase of FRB 200428 can be constrained to 11.7 mag after extinction (Lin et al. 2020). The optical band corresponding to the flux in our model is 25.7 mag, which is consistent with the true upper limit. We adopt the following parameters: $\delta t = 0.3$ s and $D = 10$ kpc. From Figure 3, the physical parameters can be constrained as follows: $\epsilon_e = 0.184_{-0.017}^{+0.004}$, $\epsilon_B = 0.015_{-0.003}^{+0.012}$, $\gamma_1 = 1.505_{-0.005}^{+0.077}$, $\gamma_2 = 26.80_{-0.34}^{+3.50}$, $p = 2.117_{-0.012}^{+0.002}$, $\log_{10}(N_e) = 42.99_{-0.02}^{+0.01}$, $\log_{10}(\ell_X/\text{cm}) = 5.457_{-0.001}^{+0.010}$, $kT = 5.624_{-0.068}^{+0.001}$ keV, $\log_{10}(E_{\text{shell}}/\text{erg}) = 40.90_{-0.07}^{+0.08}$ and $\log_{10}(n_H/\text{cm}^{-2}) = 22.25_{-0.01}^{+0.01}$. According to the fitting parameters, we can get the corresponding parameters: $\nu_m = 1.28 \times 10^{12}$ Hz, $\nu_a = 5.06 \times 10^{17}$ Hz, $\nu_c = 1.46 \times 10^{18}$ Hz, $M_{\text{shell}} = 8.83 \times 10^{19}$ g, $R_{\text{int}} = 4.09 \times 10^{10}$ cm and $B = 232.8$ G.

In our model, when the asteroid collides with the magnetar surface, a hot fireball with electrons and baryons is generated with a high temperature T_0 estimated by Equation (6). The initial temperature of the fireball determines the relativistic expansion in the later stage due to adiabatic expansion. As the fireball expands, the size and temperature of the fireball begin to evolve (see Section 2.1). Thermal X-rays from a photosphere in the relativistically expanding fireball are emitted. In Section 2.1, we calculated the blackbody temperature and the size of expanding fireball. The Thomson optical depth becomes thin when the fireball expands to the size of $\ell_X \simeq 3.5 \times 10^5$ cm. We obtain the temperature at the radius of the photosphere $kT \simeq 7$ keV at 5×10^7 cm, and find that the size and temperature of the expanding fireball are consistent with the fitting results.

During the fireball expansion, the Lorentz factor of the fireball is also evolving (see Section 2.1). First, the Lorentz factor of the fireball increases with R . When the fireball reaches its maximum acceleration radius, the fireball will keep moving at a constant Lorentz factor. According to the conservation of energy, we calculate the Lorentz factor of the ejected shell γ_{shell} . In this section, we fit the Lorentz factors of the fast and

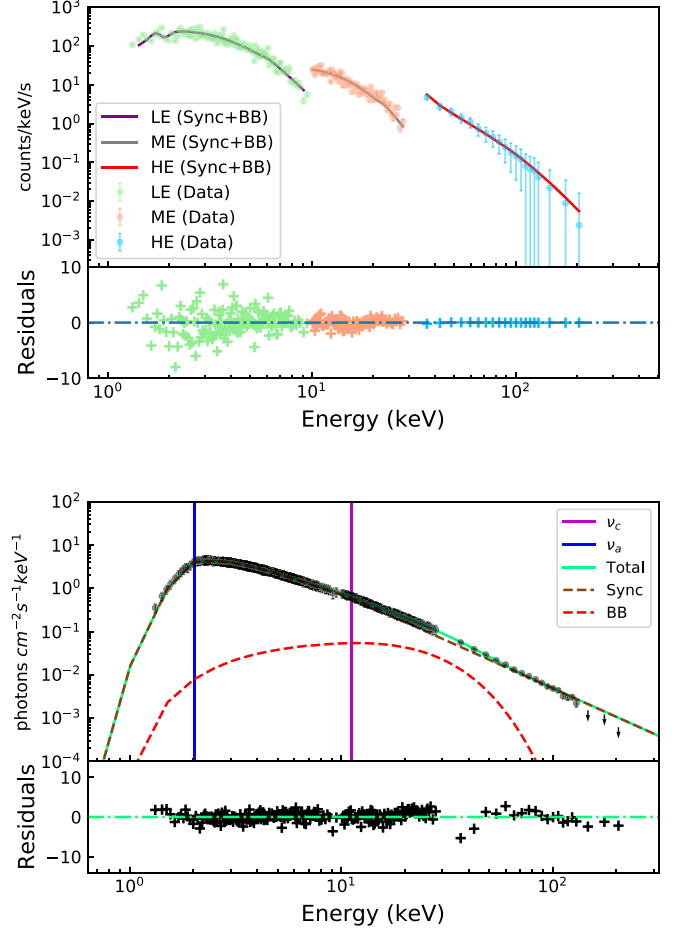


Figure 2. The spectrum of the XRB associated with FRB 200428 from SGR J1935+2154. We adopt the data observed with Insight-HXMT (Li et al. 2021). (Top) The observed photon count spectrum over-plotted with the best-fit model and residuals. (Bottom) The panel shows the de-convolved photon spectrum, and the data points represent the “observed” photon flux which is obtained by de-convolving the observed count spectrum using instrument responses. The synchrotron radiation model can fit the spectrum corresponding to the slow cooling case plus a blackbody component. The solid green, red and brown dashed lines signify the total, blackbody emission and synchrotron emission, respectively. The blue and purple solid lines represent the synchrotron self-absorption frequency and cooling frequency, respectively. The residuals are defined as (data-model)/error.

slow shells and find that the Lorentz factor of the shell is comparable to γ_{shell} . Since the components of multipolar fields are from the magnetar surface, differences would exist in the magnetic field. Therefore, the Lorentz factor of the ejected shell would have some differences when forming the fast and slow shells.

Moreover, collisions between fast and slow shells in the fireball will cause synchrotron emission. The confined shell collision radius R_{int} is larger than the photosphere radius, demonstrating that our model is self-consistent. We fit the spectrum of the XRB well to constrain reasonably other

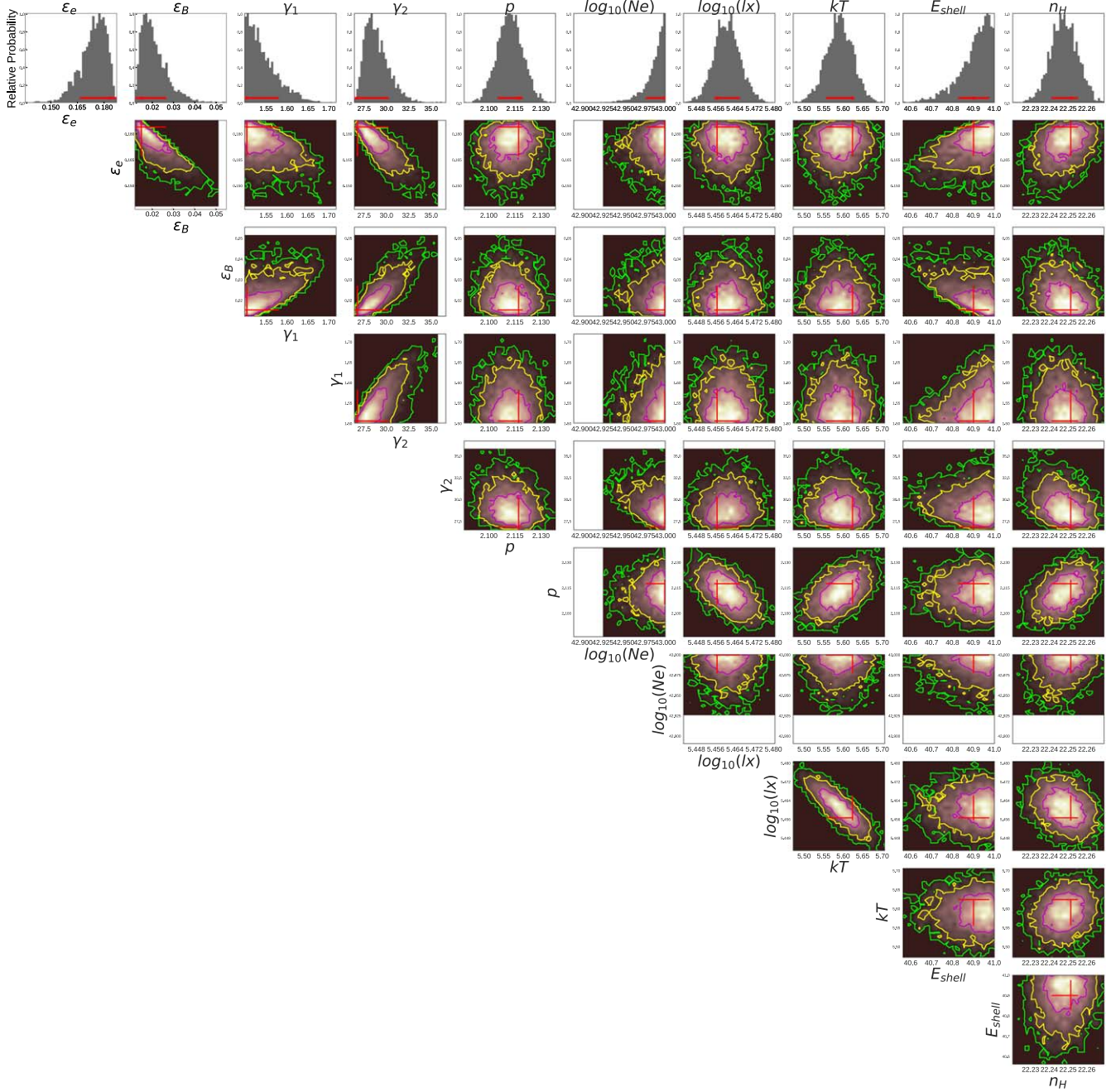


Figure 3. Corner plot of our model parameters. Histograms and contours are the log-likelihood of the parameter constraints by the McSpecFit package (Zhang et al. 2016), which shows one and two-dimensional posterior probability distributions of parameters. Red crosses mark the best-fit values and error bars are 1σ uncertainties.

parameters (e.g., p , N_e , B) in the internal shock model. In addition, the asteroid-magnetar gravitational energy contributes $\sim 10^{40}$ erg to the XRB, which is consistent with the total energy of the observed XRB from SGR J1935+2154. Figure 3 affirms that the confined shell energy and mass are comparable to the XRB energy and the fragmental mass, respectively.

4. Conclusion and Discussion

In this paper, following Dai (2020) we have proposed that the XRB associated with FRB 200428 could be generated by synchrotron emission from the internal shocks between fast and slow shells formed by a relativistically expanding fireball and constrain the model parameters. The model parameters and conclusions are summarized as follows.

1. In our model, the blackbody emission of the XRB spectrum could be contributed by an expanding fireball at the photosphere radius. Moreover, we can constrain the initial size of the trapped fireball, $\ell_{0,X} \simeq 1.3 \times 10^4$ cm. Then, the fireball will expand along magnetic field lines to the size of $\ell_X \simeq 3.5 \times 10^5$ cm, and we can get the blackbody temperature $kT \simeq 7$ keV, which is consistent with observations of the XRB (Mereghetti et al. 2020; Li et al. 2021; Ridnaia et al. 2021; Tavani et al. 2021).
2. Subsequently, collisions between fast and slow shells in the relativistic fireball could generate internal shocks and synchrotron emission. We consider the internal shock model to constrain the physical parameters.

Interestingly, the onset of the XRB is tens of milliseconds ahead of the FRBs (Mereghetti et al. 2020; Li et al. 2021; Ridnaia et al. 2021; Tavani et al. 2021). Such observation is understandable well based on our physical processes. After an asteroid is disrupted tidally into some fragments, those disrupted small fragments would fall toward the magnetar's surface earlier to contribute to the onset of the XRB, and then one of two major fragments crosses magnetic field lines at the Alfvén radius to generate a pulse of the FRB. This observation would provide strong evidence in favor of our model. In addition, Dai (2020) found that the FRB energy is proportional to $m_a^{119/81}$, and the ratio of radio and XRB energies $E_{\text{radio}}/E_X \propto m_a^{38/81}$. Therefore, the difference in the asteroidal mass may affect this ratio.

The spectrum becomes hard at the two peaks observed by Insight-HXMT (Li et al. 2021), implying that more high-energy electrons can be generated. In our model, collisions between different shells in the fireball lead to electrons being accelerated to high energy, forming more high-energy electrons. The physical process corresponds to the evolution of the spectrum from soft to hard. Moreover, in the internal shock model, the combined shells can continue colliding with other shells, leading to weaker bursts. Our model may have important implications for why there were some weaker spikes after the two peaks were observed by Insight-HXMT (Li et al. 2021).

We briefly discuss the spectrum of radiation escaping the photosphere of a fireball under strong magnetic fields. The spectrum from the trapped fireball that formed during the SGR outburst can be described by Lyubarsky (2002): $N(\epsilon) \propto \epsilon^2 \{\exp(\epsilon^2/T_{\text{eff}} \sqrt{\epsilon^2 + (3\pi^2/5)T_{\text{eff}}^2}) - 1\}^{-1}$. The spectrum is flat at low energy ($\epsilon < T_{\text{eff}} \simeq 10$ keV) because of the energy dependence of radiation cross-sections under strong magnetic fields. The spectrum is strongly distorted when radiation propagates through the magnetosphere. Notably, Yamasaki et al. (2022) considered the XRB spectrum from the trapped fireball emission reprocessed by a single resonant cyclotron scattering to be unable to explain the hard spectral index of the FRB 200428-associated burst. If there is an extremely dense magnetosphere, it could generate multiple resonant scatterings to form the hard spectrum. However, Li

et al. (2021) reported that the two-temperature blackbody model can be easily rejected, but the blackbody plus power law model can fit the FRB 200428-associated burst spectrum well. A non-thermal component and a part of the contribution from a blackbody dominate the XRB spectrum. Therefore, we further considered an XRB that can be produced by synchrotron emission from the internal shocks to fit the non-thermal component of the XRB spectrum. We found that the thermal component of the XRB spectrum fitted by Yamasaki et al. (2022) is consistent with Section 2.1.

Furthermore, recent observations indicate that some repeating FRBs manifest periodic activity (CHIME/FRB Collaboration et al. 2020; Rajwade et al. 2020; Pastor-Marazuela et al. 2021; Pleunis et al. 2021). These observations can also be explained in the pulsar-asteroid impact model of Dai et al. (2016). Periodicity in FRB 121102 and FRB 180916.J0158+65 can be explained by the orbital period of a pulsar and a stellar-mass companion, and extragalactic asteroid belt parameters can be constrained well (Dai & Zhong 2020). In addition, some repeating FRBs show the time-frequency downward drifting patterns (Caleb et al. 2020), and nearly 100% linear polarization (Day et al. 2020). The frequency drifting is mainly caused by the geometric structure of a pulsar magnetosphere, and the linear polarization can be constrained (Liu et al. 2020).

Acknowledgments

We are grateful to Fa-Yin Wang, He Gao, Tong Bao, Shu-Qing Zhong and Jun Yang for their helpful discussions and constructive comments. This work was supported by the National Key Research and Development Program of China (Grant Nos. 2017YFA0402600, 2018YFA0404204), the National SKA Program of China (Grant No. 2020SKA0120300), the National Natural Science Foundation of China (NSFC, Grant Nos. 11833003, U2038105) and the Program for Innovative Talents, Entrepreneur in Jiangsu. Y.P.Y. is supported by the National Natural Science Foundation of China (NSFC, Grant No. 12003028) and Yunnan University (Grant No. C176220100087). C.K.L. thanks support from the National Natural Science Foundation of China (NSFC, Grant No. U1838113). B.B.Z. acknowledges support by Fundamental Research Funds for the Central Universities (14380046), the National Key Research and Development Programs of China (2018YFA0404204), the National Natural Science Foundation of China (NSFC, Grant Nos. 11833003 and U2038105), the science research grants from the China Manned Space Project with NO.CMS-CSST-2021-B11, and the Program for Innovative Talents, Entrepreneur in Jiangsu.

References

- Beloborodov, A. M. 2017, *ApJL*, 843, L26
 Beloborodov, A. M. 2020, *ApJ*, 896, 142
 Beniamini, P., & Kumar, P. 2020, *MNRAS*, 498, 651
 Bochenek, C. D., Ravi, V., Belov, K. V., et al. 2020, *Natur*, 587, 59
 Boer, M., Hameury, J. M., & Lasota, J. P. 1989, *Natur*, 337, 716

- Buchner, J., Georgakakis, A., Nandra, K., et al. 2014, *A&A*, 564, A125
- Caleb, M., Stappers, B. W., Abbott, T. D., et al. 2020, *MNRAS*, 496, 4565
- CHIME/FRB Collaboration, Amiri, M., Andersen, B. C., Bandura, K. M., et al. 2020, *Natur*, 582, 351
- CHIME/FRB Collaboration, Andersen, B. C., Bandura, K. M., et al. 2020b, *Natur*, 587, 54
- Colgate, S. A., & Petschek, A. G. 1981, *ApJ*, 248, 771
- Cordes, J. M., & Wasserman, I. 2016, *MNRAS*, 457, 232
- Dai, Z. G. 2020, *ApJL*, 897, L40
- Dai, Z. G., & Lu, T. 2002, *ApJ*, 580, 1013
- Dai, Z. G., Wang, J. S., Wu, X. F., & Huang, Y. F. 2016, *ApJ*, 829, 27
- Dai, Z. G., & Zhong, S. Q. 2020, *ApJL*, 895, L1
- Day, C. K., Deller, A. T., Shannon, R. M., et al. 2020, *MNRAS*, 497, 3335
- Decoene, V., Kotera, K., & Silk, J. 2021, *A&A*, 645, A122
- Gaensler, B. M. 2014, GRB Coordinates Network, 16533, 1
- Gao, H., Lei, W.-H., Zou, Y.-C., et al. 2013, *NewAR*, 57, 141
- Geng, J.-J., Li, B., Li, L.-B., et al. 2020, *ApJL*, 898, L55
- Ghisellini, G. 2017, *MNRAS*, 465, L30
- Ghisellini, G., & Locatelli, N. 2018, *A&A*, 613, A61
- Granot, J., Ramirez-Ruiz, E., Taylor, G. B., et al. 2006, *ApJ*, 638, 391
- Gruzinov, A., & Waxman, E. 2019, *ApJ*, 875, 126
- Howard, W. M., Wilson, J. R., & Barton, R. T. 1981, *ApJ*, 249, 302
- Ioka, K. 2020, *ApJL*, 904, L15
- Israel, G. L., Esposito, P., Rea, N., et al. 2016, *MNRAS*, 457, 3448
- Katz, J. I. 2018, *MNRAS*, 481, 2946
- Katz, J. I., Toole, H. A., & Unruh, S. H. 1994, *ApJ*, 437, 727
- Keane, E. F., Stappers, B. W., Kramer, M., & Lyne, A. G. 2012, *MNRAS*, 425, L71
- Kobayashi, S., & Zhang, B. 2003, *ApJL*, 582, L75
- Kothes, R., Sun, X., Gaensler, B., et al. 2018, *ApJ*, 852, 54
- Kumar, P., Lu, W., & Bhattacharya, M. 2017, *MNRAS*, 468, 2726
- Lin, L., Zhang, C. F., Wang, P., et al. 2020, *Natur*, 587, 63
- Li, C. K., Lin, L., Xiong, S. L., et al. 2021, *NatAs*, 5, 378
- Liu, Z.-N., Wang, W.-Y., Yang, Y.-P., & Dai, Z. G. 2020, *ApJ*, 905, 140
- Livio, M., & Taam, R. E. 1987, *Natur*, 327, 398
- Lorimer, D. R., Bailes, M., McLaughlin, M. A., Narkevic, D. J., & Crawford, F. 2007, *Sci*, 318, 777
- Lu, W., & Kumar, P. 2019, *MNRAS*, 483, L93
- Lu, W., Kumar, P., & Zhang, B. 2020, *MNRAS*, 498, 1397
- Lyubarsky, Y. 2014, *MNRAS*, 442, L9
- Lyubarsky, Y. 2021, *Univ*, 7, 56
- Lyubarsky, Y. E. 2002, *MNRAS*, 332, 199
- Margalit, B., Metzger, B. D., & Sironi, L. 2020, *MNRAS*, 494, 4627
- Mereghetti, S., Savchenko, V., Ferrigno, C., et al. 2020, *ApJL*, 898, L29
- Metzger, B. D., Margalit, B., & Sironi, L. 2019, *MNRAS*, 485, 4091
- Mitrofanov, I. G., & Sagdeev, R. Z. 1990, *Natur*, 344, 313
- Paczynski, B., & Xu, G. 1994, *ApJ*, 427, 708
- Pastor-Marazuela, I., Connor, L., van Leeuwen, J., et al. 2021, *Natur*, 596, 505
- Pavlović, M. Z., Urošević, D., Vukotić, B., et al. 2013, *ApJS*, 204, 4
- Platts, E., Weltman, A., Walters, A., et al. 2019, *PhR*, 821, 1
- Pleunis, Z., Michilli, D., Bassa, C. G., et al. 2021, *ApJL*, 911, L3
- Rajwade, K. M., Mickaliger, M. B., Stappers, B. W., et al. 2020, *MNRAS*, 495, 3551
- Rees, M. J., & Meszaros, P. 1994, *ApJL*, 430, L93
- Ridnaia, A., Svinikin, D., Frederiks, D., et al. 2021, *NatAs*, 5, 372
- Sari, R., & Piran, T. 1999, *ApJ*, 520, 641
- Sari, R., Piran, T., & Narayan, R. 1998, *ApJL*, 497, L17
- Shull, J. M., & Stern, S. A. 1995, *AJ*, 109, 690
- Surnis, M. P., Joshi, B. C., Maan, Y., et al. 2016, *ApJ*, 826, 184
- Tavani, M., Casentini, C., Ursi, A., et al. 2021, *NatAs*, 5, 401
- Thompson, C., & Duncan, R. C. 1995, *MNRAS*, 275, 255
- Thompson, C., & Duncan, R. C. 2001, *ApJ*, 561, 980
- Thornton, D., Stappers, B., Bailes, M., et al. 2013, *Sci*, 341, 53
- van Buren, D. 1981, *ApJ*, 249, 297
- Wadiasingh, Z., Beniamini, P., Timokhin, A., et al. 2020, *ApJ*, 891, 82
- Wadiasingh, Z., & Timokhin, A. 2019, *ApJ*, 879, 4
- Wang, W.-Y., Xu, R., & Chen, X. 2020, *ApJ*, 899, 109
- Wang, W. Y., Zhang, B., Chen, X. L., & Xu, R. X. 2019, *ApJL*, 876, L15
- Waxman, E. 2017, *ApJ*, 842, 34
- Wu, Q., Zhang, G. Q., Wang, F. Y., et al. 2020, *ApJL*, 900, L26
- Xiao, D., & Dai, Z.-G. 2020, *ApJL*, 904, L5
- Xiao, D., Wang, F. Y., & Dai, Z.-G. 2020, *SCPMA*, 64, 249501
- Yamasaki, S., Kashiyama, K., & Murase, K. 2022, *MNRAS*, 511, 3138
- Yang, Y.-P., & Zhang, B. 2018, *ApJ*, 868, 31
- Yang, Y.-P., & Zhang, B. 2021, *ApJ*, 919, 89
- Yang, Y.-P., Zhu, J.-P., Zhang, B., et al. 2020, *ApJL*, 901, L13
- Younes, G., Baring, M. G., Kouveliotou, C., et al. 2021, *NatAs*, 5, 408
- Younes, G., Güver, T., Kouveliotou, C., et al. 2020, *ApJL*, 904, L21
- Zhang, B. 2017, *ApJL*, 836, L32
- Zhang, B. 2020, *ApJL*, 890, L24
- Zhang, B. 2020, *Natur*, 587, 45
- Zhang, B., & Mészáros, P. 2002, *ApJ*, 581, 1236
- Zhang, B.-B., Uhm, Z. L., Connaughton, V., et al. 2016, *ApJ*, 816, 72
- Zhong, S.-Q., Dai, Z.-G., Zhang, H.-M., et al. 2020, *ApJL*, 898, L5
- Zhou, P., Zhou, X., Chen, Y., et al. 2020, *ApJ*, 905, 99